Journal of Nuclear Medicine, published on September 14, 2017 as doi:10.2967/jnumed.116.187666

Performance of a PET Insert for High Resolution Small Animal PET/MR Imaging at 7T

Greg Stortz[1]
Jonathan D. Thiessen[2,3]
Daryl Bishop[4]
Muhammad Salman Khan[5]
Piotr Kozlowski[6]
Fabrice Retière[4]
Graham Schellenberg[7]
Ehsan Shams[8]
Xuezhu Zhang[9,10]
Christopher J. Thompson[11]
Andrew L. Goertzen[9,7,†]
Vesna Sossi[1,†]

[†]Andrew Goertzen and Vesna Sossi are co-equal senior authors

[1]Department of Physics & Astronomy at the University of British Columbia, Vancouver, BC, Canada
[2]Department of Medical Biophysics, Western University, London, ON, Canada
[3]Graduate Program in Biomedical Engineering, University of Manitoba, Winnipeg, MB, Canada
[4]Detector Development Group, TRIUMF, Vancouver, BC, Canada
[5]Department of Electrical Computer Engineering, University of Manitoba, Winnipeg, MB, Canada
[6]Department of Radiology, University of British Columbia, Vancouver, BC, Canada
[7]Department of Physics & Astronomy, University of Manitoba, Winnipeg, MB, Canada
[8]Biomedical Engineering Graduate Program, University of Manitoba, Winnipeg, MB, Canada
[9]Department of Radiology, University of Manitoba, Winnipeg, MB, Canada
[10]Department of Biomedical Engineering, University of California, Davis, Davis, CA, USA
[11]Montreal Neurological Institute, McGill University, Montreal, QC, Canada

First author:
Greg Stortz (PhD student during authorship)
The Hospital for Sick Children

Corresponding authors:
Greg Stortz: email: greg.stortz@alumni.ubc.ca
Andrew L. Goertzen: Andrew.Goertzen@umanitoba.ca

Word count: 4994

Financial Support:

Mitacs Accelerate Cluster Grant IT04494
NSERC Discovery Grants 36672, 341628 and 240670
University of Manitoba Amalgamated Research Fund.

Short title: PET/MR Insert Characterization

ABSTRACT

We present the characterization of a compact magnetic resonance (MR) compatible positron emission tomography (PET) insert for simultaneous pre-clinical PET/MR imaging. While specifically designed with the strict size constraint to fit inside the 114 mm inner diameter of the BGA-12S gradient coil used in the Bruker 70/20 and 94/20 series of small animal MR imaging (MRI) systems, the insert can be easily installed in any appropriate MRI scanner or used as a stand-alone PET system.

Methods

The insert is made from a ring of 16 detector-blocks each made from depth-of-interaction capable dual-layer-offset arrays of cerium-doped lutetium-yttrium oxyorthosilicate crystals read out by silicon photomultiplier (SiPM) arrays. Scintillator crystal arrays are made from 22×10 / 21×9 crystals in the bottom/top layers with 6/4 mm layer thicknesses, arranged with a 1.27 mm pitch, resulting in a useable field of view (FOV) 28 mm long and ~55 mm wide.

Results

Spatial resolution ranges from 1.17 to 1.86 mm full-width-at-half-maximum (FWHM) in the radial direction from a radial offset of 0 to 15 mm. With a 300-800 keV energy window, peak sensitivity is 2.2% and noise-equivalent count rate (NECR) from a mouse-sized phantom at 3.7 MBq is 11.1 kcps and peaks at 20.8 kcps at 14.5 MBq. Phantom imaging shows that feature sizes as low as 0.7 mm can be resolved. ^{18}F-fluorodeoxyglucose (^{18}F-FDG) PET/MR images of mouse and rat brains show no signs of inter-modality interference, and can excellently resolve substructures within the brains.

Conclusions

Due to excellent spatial resolvability and lack of intermodality interference, this PET insert will serve as a useful tool for pre-clinical PET/MR.

INTRODUCTION

PET allows for functional in-vivo imaging of a positron-emitting radiotracer. While its strength lies in the ability to accurately detect radioisotopes at picomolar concentrations in-vivo (*1*), PET does not provide anatomical information. Hybrid PET systems incorporating x-ray computed tomography (PET/CT) or MRI (PET/MR) dramatically increase the value of PET by providing an anatomical backdrop to PET images.

While PET/CT is a mature clinical and pre-clinical technology, PET/MR is still an emerging technology. PET/MR has traditionally been a challenge because the photomultiplier tubes that detect scintillation light cannot function inside of a strong magnetic field. Early attempts at simultaneous PET/MR for clinical (*2-4*) and pre-clinical applications (*5,6*) used fiber-optic cables to direct scintillation light to photomultiplier tubes positioned outside the magnetic field. In addition to signal distortion and energy resolution degradation due to light-loss, the volume of fiber-optic cabling created space constraints limiting the number of detectors.

Later work used MR-compatible avalanche photodiodes to directly read-out scintillator crystals inside an MRI (*7-10*). Compared to photomultiplier tubes, avalanche photodiodes result in poorer timing resolution and low, temperature sensitive gain (*11*). SiPMs have recently become an attractive alternative to avalanche photodiodes for PET/MR (*12-14*) because they offer gain and timing resolution comparable to photomultiplier tubes while also functioning in strong magnetic fields with little temperature dependence (*11,15,16*).

This work presents a SiPM based MR-compatible high-resolution PET insert allowing for simultaneous PET/MR imaging of small animals. An *insert* is advantageous to integrated PET/MR systems because it can be retrofit to existing MRI scanners, potentially reducing the capital cost by a large factor for groups pursuing simultaneous PET/MR, while also functioning as a compact stand-alone PET system. Our design was constrained so that the insert could fit inside of a Bruker BGA-12S gradient coil (inner diameter 114 mm) installed in both 70/20 and 94/20 models of the Bruker BioSpec preclinical MRI. The inner bore of the PET insert was required to be large enough to accommodate the 60 mm outer diameter of the Bruker 35 mm radiofrequency volume coil. The resulting high curvature of the PET detector ring exacerbates resolution degradation from the parallax effect, as annihilation photons originating from even a small radial offset will enter the detectors at a substantial angle. Our PET system was therefore built using depth-of-

interaction capable detectors to mitigate the parallax effect.

We previously reported on the MR-compatibility of the PET insert (*17*), and have shown the first images and a preliminary characterization (*18*). Here we present a final characterization of the PET insert following major firmware updates that yielded substantial improvements in signal timing accuracy and count rate performance and therefore superior image quality. Additionally, a point-spread-function modeling maximum-likelihood / expectation-maximization (PSF-MLEM) algorithm tailored to this PET detector geometry (*19*) was used for the first time to reconstruct phantom and rodent data.

MATERIALS AND METHODS

PET Insert Description

Each detector-block consists of a dual-layer-offset array (*20,21*) of cerium-doped lutetium-yttrium oxyorthosilicate crystals read-out by two SensL ArraySB-4 SiPM arrays (SensL Inc., Cork, Ireland). Crystal arrays (Proteus Inc, Chagrin Falls, OH) are made from 22×10 (1.2×1.2×6 mm^3) crystals in the bottom layer and 21×9 (1.2×1.2×4 mm^3) crystals in the top layer. Crystals are polished and coated in enhanced specular reflector film bonded with Dymax OP-20 UV curing glue and arranged with a 1.27 mm pitch as shown in Fig. 1a. A 1.0 mm thick glass light-guide allows scintillation light to diffuse before reaching the SiPMs. The 32 SiPM analog outputs are multiplexed to four by a resistive charge division network (*22,23*). Analog outputs are carried from each detector-block by high definition multimedia interface cables, which also power the SiPMs (*24*).

Sixteen detector-blocks were mounted to copper-clad printed circuit boards, which are mounted to plastic supports secured to a 60 mm wide carbon-fiber tube. The geometry of the PET insert is summarized in Table 1. Fig. 1b shows an assembled detector-block mounted. Fig. 2a shows the partially assembled gantry, making visible the 35 μm thick copper foil on the printed circuit boards and lining the inside of the gantry for radiofrequency shielding from the MRI (*17*). The assembled gantry was sheathed in a woven carbon-fiber tube (Rockwest Composites, West Jordan, UT) and closed with machined plastic caps (Fig. 2b).

Four detector support boards supply power to the detectors and relay analog signals to detector boards in an OpenPET data acquisition system (*25,26*) via a 96-pin cable. The OpenPET system triggers based on a voltage threshold, after which digitized (peak minus baseline) time-stamped signals are reported back to an

acquisition computer via universal serial bus 2.0. OpenPET firmware was highly customized to output 8-byte singles packets, allowing acquisition of singles at rates up to 5 Mcps.

Data Processing

Crystal identification and coincidence detection are performed retrospectively in software. An automated algorithm to segment flood histograms allows for rapid generation of crystal- and energy-look-up-tables (*27*) used for crystal identification and energy discrimination (with a 300 to 800 keV window). The coincidence window was set to 10 ns (appropriate for the measured 5.4 ns singles timing resolution). Randoms rates are estimated using a delayed coincidence window.

Each crystal pair is mapped to a sinogram bin using nearest-neighbor interpolation to evenly spaced radial and angular intervals. Complex geometric factors following from the dual-layer-offset detector design result in a situation where it is not possible to employ conventional axial mashing approaches (as described by *Michelograms* (*28*)) to create a single set of sinograms, so an alternative method was developed (*29*). In this work, sinograms are formed using 67 radial bins, 104 views, a span of three and a maximum ring difference of 19. Reconstructed sinograms are normalized with component-based-normalization. Analytic reconstruction is performed using the filtered back projection / 3D reprojection (FBP-3DRP) algorithm as implemented in the open-source reconstruction suite STIR 3.0 (software for tomographic image reconstruction) (*30*).

PSF-MLEM Algorithm

An LOR-based PSF-modeling MLEM algorithm developed *in-house* was previously shown to produce very high contrast images when tested on simulated data (*19*), however without incorporation of normalization. Because the PSF-MLEM system matrix accounts for many of the geometric factors that would be included in component-based-normalization, normalization factors must be different than for FBP. In an approach similar to that of Bai, *et al* (*31*), the system matrix was used to forward project a known distribution of activity (a thin-walled annulus) so that the geometric factors incorporated in the system matrix could be determined and removed from the normalization factors.

Further modifications to the algorithm were made to remove persistent non-uniformity artefacts (*28*), resulting in a drastic increase in reconstruction time (25 iterations taking over one year with work split between 20 threads running on a PC with four twelve-core AMD Opteron 6192 CPUs). Identification of

massive symmetries in the system matrix allowed for <1% of non-zero system matrix elements to be calculated and the rest populated using these symmetries. Instead of using *on-the-fly* calculation, this small fraction of system matrix elements was computed once and saved to disk (occupying 1.5 or 5.8 GB of storage space for zoom-1 or -2 reconstructions, respectively) to be recalled during reconstruction, producing a more practical reconstruction time (25 or 105 minutes per iteration for zoom-1 or -2). Although not yet been implemented, the ordered-subset-expectation-maximization algorithm could further accelerate reconstruction time. For images shown in this paper, iterations were performed until there was no further visual improvement in image contrast.

PET System Performance

The PET insert was characterized in terms of spatial resolution, sensitivity, and NECR closely following the methods prescribed by the NEMA NU 4-2008 protocol (*32*). Phantom images along with mouse and rat ^{18}F-FDG images further illustrate the performance of the PET insert. Rodent imaging was performed in the 7 T Bruker MRI as MR images were acquired.

Spatial Resolution. A 0.49 MBq 0.25 mm diameter spherical ^{22}Na source embedded in a 1.0 cm wide acrylic cube (Model MMS09, Eckert & Ziegler Isotope Products, Valencia, CA) was scanned at radial offsets of 0, 5, 10, and 15 mm at the axial center and again offset from the axial center by one quarter the length of the FOV with at least 10^6 coincidences acquired per position. Source movement was enabled by a motorized stage with a positioning accuracy of ~15 μm over 5 cm of motion (seen in Fig. 2b; Model MN10-150-M02-21, Velmex, Bloomfield, NY). From reconstructed FBP-3DRP images (voxel size 0.159×0.159×0.635 mm^3) the FWHM and full-width-at-tenth-maximum was determined according to the protocol defined by the NEMA NU 4-2008 standard. Volumetric resolution (the product of FWHM in the three orthogonal directions) was also calculated.

Sensitivity. A ^{22}Na source like the one used to measure resolution but with an activity of 125 kBq was stepped along the axis of the PET scanner with a step size of 0.635 mm (half the crystal pitch) using the motorized stage, with 30 s of data acquired at each position. Randoms-corrected sinograms for each source position were formed, and for each view all sinogram bins further than 1.0 cm from the highest-count bin were set to zero. The number of counts remaining in all sinograms were summed and divided by the

acquisition time to yield the count rate *C*. From this, sensitivity was calculated as:

$$Sensitivity = \frac{C}{\gamma A} \quad (1)$$

where γ is the branching ratio of ^{22}Na for positron decay, and A is the source activity. Sensitivity is plotted as a function of source position along the scanner axis.

NECR and Scatter Fraction. NECR was measured according to the NEMA NU 4-2008 protocol using the mouse-sized count rate phantom. Beginning with approximately 40 MBq of ^{18}F, data were collected using 10 minute long frames once per hour for 14 hours. Sinograms of prompt and delayed coincidences were created, and from these, rates of true (T), random (R) and scattered coincidences (S) were determined and NECR was calculated according to:

$$NECR = \frac{T^2}{T + S + 2R} \quad (2)$$

Scatter fraction (S/(T+S)) is reported for a source activity of 3.2 MBq.

Phantom Images. Two phantoms were imaged in order to demonstrate the image quality achievable with this PET system: the NEMA NU 4-2008 image quality phantom and a micro-resolution phantom (MI Labs Model 850.500, MI Labs, Utrecht, The Netherlands). The 58 mm long image quality phantom was filled with 8.6 MBq of ^{18}F and scanned in a three-step step-and-shoot acquisition for 20 minutes per bed position, enabled by the motorized stage. This step-and-shoot protocol was repeated four times, and data sets for the same bed position were appended together. We chose to scan at a higher activity and for a longer period of time than what is prescribed by NEMA NU 4-2008 to avoid a very low-count data set due to low sensitivity and the need to scan in three bed-positions. The micro-resolution phantom, which has an axial length of 12 mm, was scanned in one 60-minute acquisition after being filled with 8.7 MBq of ^{18}F. The phantom contains groups of rods with diameters of 0.7, 0.8, 0.9, 1.0, 1.2, and 1.5 mm. Center-to-center spacing is twice the rod diameter.

Data were reconstructed with FBP-3DRP and the aforementioned PSF-MLEM method. The FBP

reconstruction of the NEMA image quality phantom was analyzed according to the NEMA NU 4-2008 protocol to quantify uniformity, recovery coefficients (mean image value along the center of the rods divided by mean image value in the uniformity region), and spill-over ratio (mean value in each of the cold inserts divided by mean value in the uniformity region).

Rodent Images. Simultaneous PET/MR images of both a mouse and a rat were acquired and are presented in this paper to demonstrate the intended use of the PET system. The PET system was centered inside of the MRI gradient coil. 4.47 MBq of ^{18}F-FDG was administered to a 40.1 g 3xTG mouse by intraperitoneal injection (preferred to intravenous injection due to higher success rate). After a one hour long uptake period, acquisition of PET and MRI data commenced with the mouse brain centered in the FOV with an 18 mm × 22 mm flat quadrature surface coil positioned above the brain. Half-Fourier-acquisition-single-shot-turbo-spin-echo MRI acquisitions ran for the entirety of the 20 min PET acquisition. Resulting 128×128 MR images had an in-plane resolution of 0.15875 mm.

14.8 MBq of ^{18}F-FDG was administered to a 270 g Sprague-Dawley rat by intravenous injection. A custom-built radiolucent radiofrequency volume coil (*33*) was placed inside of the PET system, with the rat's brain centered in the FOV. Simultaneous PET/MR imaging began after a 50 minute uptake period. Half-Fourier-acquisition-single-shot-turbo-spin-echo acquisitions were run for the entirety of the 30 min long PET acquisition resulting in 128×128 images with in-plane resolution of 0.3175 mm.

RESULTS

The reconstructed spatial resolution throughout the FOV is summarized in Tables 1 and 2. In the axial center of the FOV, radial FWHM ranges from 1.17 to 1.86 mm between the radial center to a 15 mm offset and volumetric resolution ranges from 2.15 to 4.06 μL.

The sensitivity profile follows a characteristic triangular shape, and peaks at 2.2% (Fig. 3). Firmware updates lead to an improvement to the previously observed sensitivity of 1.9%. The sensitivity was previously reported inaccurately as 1.3% in (*18*) due to source activity misreporting by the manufacturer. Fig. 4 shows the mouse-NECR as a function of source activity, along with corresponding rates of trues, scatters, and randoms. NECR at 3.7 MBq is 11.1 kcps, and a peak NECR of 20.8 kcps is reached at 14.5 MBq. The scatter fraction at 3.2 MBq is 15.4%.

Zoom-1 FBP-3DRP and PSF-MLEM (30 iterations) reconstructions of the three sections of the NEMA image quality phantom are shown in Supplemental Fig. 1. All five rods are visible in the hot-rod section and the uniformity section appears uniform. Images, which are not quantitative due to lack of deadtime correction, were rescaled to have approximately the same value in regions where bed positions overlapped. Uniformity, recovery coefficients, and spill-over ratios resulting from both FBP-3DRP and PSF-MLEM reconstructions are shown in Table 4. The recovery coefficients are in general higher when using PSF-MLEM.

Fig. 5 shows zoom-2 reconstructions of the micro-resolution phantom made with FBP-3DRP (left) and 99 iterations of PSF-MLEM (right). The FBP-3DRP reconstruction resolves rod sizes as small as 0.9 mm, while the PSF-MLEM reconstruction resolves even the smallest rods, which are 0.7 mm wide. At such a high resolution that resolvable feature sizes are comparable to the average positron range (0.85 mm for ^{18}F (*34*)), further improvements to the algorithm would likely need to account for positron range in the system matrix (*35*).

Zoom-1 PSF-MLEM reconstructions of the mouse/rat brains (respectively using 21/25 iterations) are shown in Fig. 6 along with fused MR images. Corresponding FBP-3DRP reconstructions are shown in Supplemental Fig. 2. PSF-MLEM produces rodent images that are much more capable of resolving structures within the brain, showing clear separation between the cortex and the basal ganglia. As expected, regions in the MR images that are clearly identifiable as cortex correspond to high ^{18}F-FDG uptake in PET images.

DISCUSSION

An MR-compatible small animal PET insert was characterized in terms of spatial resolution, sensitivity and NECR. Spatial resolution in the center of the FOV outperforms the commonly used Siemens microPET Focus 120, Focus 220, and Inveon pre-clinical PET scanners, for which the respective radial resolution at 5 mm offsets are 1.92, 1.75, and 1.63 mm (*36*). At a 15 mm offset, these systems compare very closely to ours in terms of radial resolution (1.99, 1.82 and 2.03 mm). The spatial resolution of the MR-compatible preclinical PET insert reported by Ko, *et al* (*12*) is nominally the same as ours in the center of the FOV, but degrades with radial offset faster than ours due to lack of depth-of-interaction measurement (volumetric

resolution of 1.93 / 7.27 μL at 0 / 14 mm radial offsets). The HyperIon II (a digital-SiPM based MR-compatible PET insert) was shown to resolve a rod size only as small as 0.8 mm using an MLEM reconstruction algorithm (*14*)) – slightly below the performance of our PET system.

NECR and peak sensitivity are notably poorer than other pre-clinical PET systems - however this is largely due to the low geometric factor following from the limited axial FOV. The peak sensitivity of the Siemens microPET Focus 120, Focus 220, and Inveon are respectively 3.42, 2.28, and 6.72% (*36*) compared to 2.2% for our system when using a similar energy window. These systems have mouse-NECR at 3.7 MBq of 66.5, 47.3, and 129.0 kcps, all exceeding the 11.1 kcps that we measured. The HyperIon II has a peak sensitivity of 2.6% using a lower energy limit of 250 keV (*37*). The MR-compatible PET insert by Ko, *et al* has a reported peak sensitivity of 3.36% (*38*) and mouse-NECR at 3.7 MBq of 23.4 kcps (*12*) while using a lower energy limit of 250 keV. This sensitivity figure is comparable to our system. Analysis of singles data suggests that our system is characterized by paralyzable block-level deadtime in excess of approximately 1.3 μs. Such a large deadtime would compound with our low geometric sensitivity to explain our low NECR performance. Future versions of our PET insert design will have an axial FOV between two and three times longer than the prototype and reduced deadtime, resulting in large gains in sensitivity and NECR.

PET images acquired simultaneously with MRI and vice versa show no signs of interference. In a previous study of the MR-compatibility of our PET insert (*17*), no significant effect on the PET system due to the MRI was observed, and the PET system introduced only minor degradations in B_0 homogeneity (0.16 to 0.26 ppm) and no significant drop in image signal-to-noise-ratio during multi-slice-multi-echo, rapid-imaging-with-refocused-echoes, and fast-low-angle-shot pulse-sequences, however a 9% drop in signal-to-noise-ratio was observed for echo-planar-imaging sequences.

CONCLUSION

This MR-compatible PET insert can obtain high-resolution PET images while functioning inside of a 7T MRI with very little inter-modality interference. PET image quality is especially good when using the custom-made PSF-MLEM reconstruction software. NECR and sensitivity are low compared to most PET systems due to the short axial length of the scanner and high deadtime of the current prototype.

DISCLOSURE

The authors have no conflicts of interest to disclose.

Funded by a Mitacs Accelerate Cluster Grant IT04494 to V. Sossi and A.L. Goertzen partnered with Cubresa Inc. (Winnipeg, Canada), Natural Sciences and Engineering Research Council of Canada Discovery Grants to C.J. Thompson (36672), A.L. Goertzen (341628) V. Sossi (240670), and the University of Manitoba Amalgamated Research Fund. The radiofrequency coil used for the rat imaging was supplied by Cubresa Inc. at no cost.

ACKNOWLEDGEMENT

The authors thank Drs. Melanie Martin and Richard Buist from the University of Manitoba In-Vivo Experimental Animal Magnetic Resonance Microscopy Centre for assistance with PET/MR imaging, Dr. Michael Jackson of the University of Manitoba Small Animal and Materials Imaging Core Facility, Drs. Dali Zhang and Ji Hyun Ko from the Neuroscience Research Program at the University of Manitoba for assistance with rat imaging, Dr. Benedict Albensi from the Department of Pharmacology and Therapeutics at the University of Manitoba for supplying the mice, and Bob Miller of the Medical Devices Group at CancerCare Manitoba for assistance with PET insert gantry design and fabrication.

REFERENCES

1. Hutchins GD, Miller MA, Soon VC, Receveur T. Small animal PET imaging. *ILAR J*. 2008;49:54-65
2. Shao Y, Cherry SR, Farahani K, *et al*. Simultaneous PET and MR imaging. *Phys Med Biol*. 1997;42:1965-1970
3. Catana C, Wu Y, Judenhofer MS, *et al*. Simultaneous acquisition of multislice PET and MR images: initial results with a MR-compatible PET scanner. *J Nucl Med*. 2006;47:1968-1976
4. Farahani K, Slates R, Shao Y, *et al*. Contemporaneous positron emission tomography and MR imaging at 1.5 T. *J Magn Reson Imaging*. 1999;9:497-500
5. Raylman RR, Majewski S, Lemieux SK, *et al*. Simultaneous MRI and PET imaging of a rat brain. *Phys Med Biol*. 2006;51:6371-6379
6. Yamamoto S, Imaizumi M, Kanai Y, *et al*. Design and performance from an integrated PET/MRI system for small animals. *Ann Nucl Med*. 2010;24:89-98
7. Maramraju SH, Smith SD, Junnarkar SS, *et al*. Small animal simultaneous PET/MRI: initial experiences in a 9.4 T microMRI. *Phys Med Biol*. 2011;56:2459-2480
8. Judenhofer MS, Catana C, Swann BK, *et al*. PET/MR images acquired with a compact MR-compatible PET detector in a 7-T magnet. *Radiology*. 2007;244:807-814
9. Pichler BJ, Judenhofer MS, Catana C, *et al*. Performance test of an LSO-APD detector in a 7-T MRI scanner for simultaneous PET / MRI. *J Nucl Med*. 2006;47:639-647
10. Delso G, Furst S, Jakoby B, *et al*. Performance measurements of the Siemens mMR integrated whole-body PET/MR scanner. *J Nucl Med*. 2011;52:1914-1922
11. Roncali E, Cherry SR. Application of silicon photomultipliers to positron emission tomography. *Ann Biomed Eng*. 2011;39:1358-1377
12. Ko GB, Kim KY, Yoon HS, *et al*. Evaluation of a silicon photomultiplier PET insert for simultaneous PET and MR imaging. *Med Phys*. 2016;43:72-83
13. Yamamoto S, Watabe T, Watabe H, *et al*. Simultaneous imaging using Si-PM-based PET and MRI for development of an integrated PET/MRI system. *Phys Med Biol*. 2012;57:N1-13

14. Schug D, Lerche C, Weissler B, *et al*. Initial PET performance evaluation of a preclinical insert for PET/MRI with digital SiPM technology. *Phys Med Biol*. 2016;61:2851-2878
15. Heering A, Rohlf J, Freeman J, *et al*. Performance of silicon photomultipliers with the CMS HCAL front-end electronics. *Nucl Instrum Meth A*. 2007;576:341-349
16. Spanoudaki VC, Mann AB, Otte AN, *et al*. Use of single photon counting detector arrays in combined PET/MR: Characterization of LYSO-SiPM detector modules and comparison with a LSO-APD detector. *J Instrum*. 2007;2:P12002
17. Thiessen JD, Shams E, Stortz G, *et al*. MR-compatibility of a high-resolution small animal PET insert operating inside a 7 T MRI. *Phys Med Biol*. 2016;61:7934-7956
18. Goertzen AL, Stortz G, Thiessen JD, *et al*. First results from a high-resolution small animal SiPM PET insert for PET / MRI imaging. *IEEE T Nucl Sci*. 2016;63:2424-2433
19. Zhang X, Stortz G, Sossi V, *et al*. Development and evaluation of a LOR-based image reconstruction with 3D system response modeling for a PET insert with dual-layer offset crystal design. *Phys Med Biol*. 2013;58:8379-8399
20. Thompson CJ, Stortz G, Goertzen AL, *et al*. Comparison of single and dual layer detector blocks for pre-clinical MRI-PET. *Nucl Instrum Meth A*. 2012;702:56-58
21. Thompson CJ, Goertzen AL, Berg E, *et al*. Evaluation of high density pixellated crystal blocks with SiPM readout as candidates for PET / MR detectors in a small animal PET insert. *IEEE T Nucl Sci*. 2012;59:1791-1797
22. Goertzen AL, Zhang X, McClarty MM, *et al*. Design and performance of a resistor multiplexing readout circuit for a SiPM detector. *IEEE T Nucl Sci*. 2013;60:1541-1549
23. Liu CY, Goertzen AL. Multiplexing approaches for a 12 x 4 array of silicon photomultipliers. *IEEE T Nucl Sci*. 2014;61:35-43
24. Goertzen AL, Thiessen JD, Zhang X, *et al*. Application of HDMI ® cables as an MRI compatible single cable solution for readout and power supply of SiPM based PET detectors. *IEEE Nucl Sci Conf R*. 2012:3184-188
25. Abu-Nimeh FT, Ito J, Moses WW, *et al*. Architecture and implementation of OpenPET firmware and embedded software. *IEEE T Nucl Sci*. 2016;63:620-629

26. Moses WW, Buckley S, Vu C, *et al.* OpenPET: A flexible electronics system for radiotracer imaging. *IEEE T Nucl Sci*. 2010;57:2532-2537
27. Schellenburg G, Stortz G, Goertzen AL. An algorithm for automatic crystal identification in pixelated scintillation detectors using thin plate splines and Gaussian mixture models. *Phys Med Biol.* 2016;61:N90-101
28. Stortz G. Development of a small animal MR compatible PET Insert. 2016. PhD Thesis, University of British Columbia, Vancouver, Canada
29. Fahey FH. Data acquisition in PET imaging. *J Nucl Med Tech*. 2002;30:39-49
30. Thielemans K, Tsoumpas C, Mustafovic S, *et al*. STIR: software for tomographic image reconstruction release 2. *Phys Med Biol.* 2012;57:867-883
31. Bai B, Li Q, Holdsworth CH, *et al*. Model-based normalization for iterative 3D PET image reconstruction. *Phys Med Biol*. 2002;47:2773-2784
32. National Electrical Manufacturers Association. NEMA standard publication NU 4-2008: Performance measurements of small animal positron emission tomographs. National Electrical Manufacturers Association, Rosslyn, VA. 2008.
33. Goertzen AL, Buist R, Herrera SL, *et al*. A custom RF coil for high resolution PET/MR imaging at 7T with a PET insert. *Proceedings of the 5th Conference for PET/MR and SPECT/MR*. 2016. In press.
34. Tai YC, Laforest, R. Instrumentation aspects of PET imaging. *Annu Rev Biomed Eng.* 2005;7:255-288
35. Rahmim A, Qi J, Sossi V. Resolution modeling in PET imaging: theory, practice, benefits, and pitfalls. *Med Phys*. 2013;40:064301
36. Goertzen AL, Bao Q, Bergeron M, *et al*. NEMA NU 4-2008 comparison of preclinical PET imaging systems. *J Nucl Med*. 2012;53:1300-1309
37. Weissler B, Gebhardt P, Dueppenbecker PM, *et al*. A digital preclinical PET/MRI insert and initial results. *IEEE T Med Imaging*. 2015;34:2258-2270

38. Ko GB, Yoon HS, Kim KY, *et al*. Simultaneous multi-parametric PET/MRI with silicon photomultiplier PET and ultra-high field MRI for small animal imaging. *J Nucl Med*. 2016;57:1309-1316

FIGURES

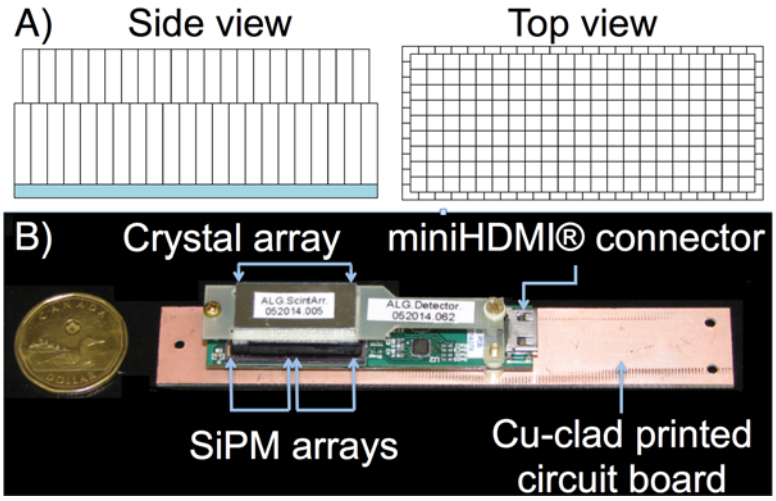

FIGURE 1. (a) Schematic of crystal array with the light-guide shown in blue. (b) Photograph of an assembled detector-block, next to a Canadian $1 coin for size comparison.

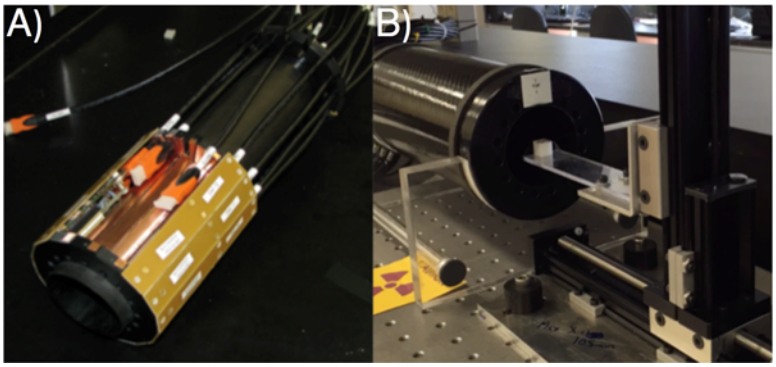

FIGURE 2. (a) The partially assembled ring of PET detector-blocks and (b) the assembled PET insert.

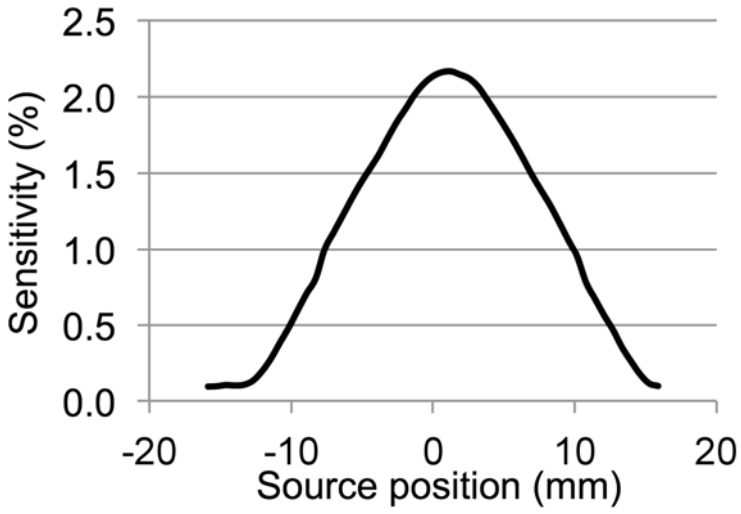

FIGURE 3. Axial sensitivity profile.

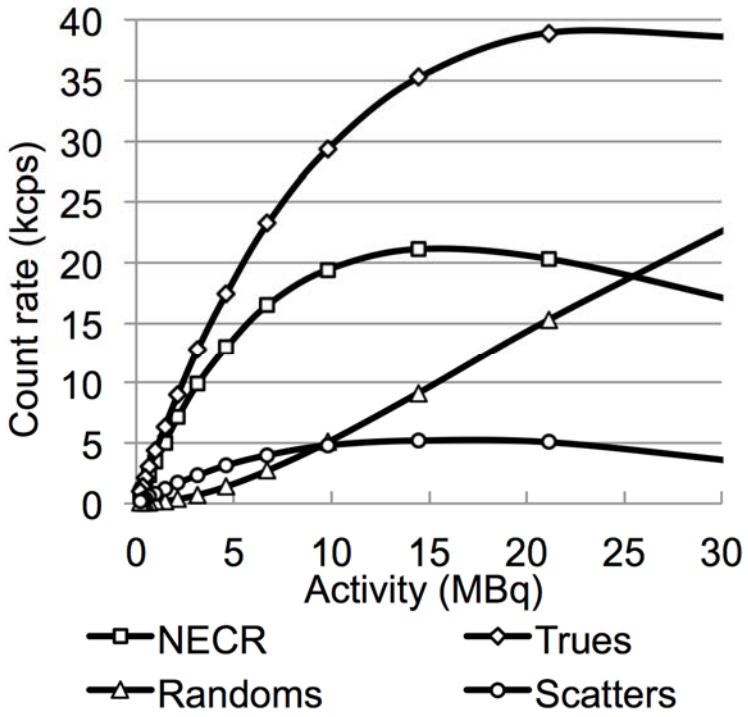

FIGURE 4. NECR as a function of source activity for the NEMA mouse-size phantom, with corresponding rates of trues, randoms, and scattered coincidences.

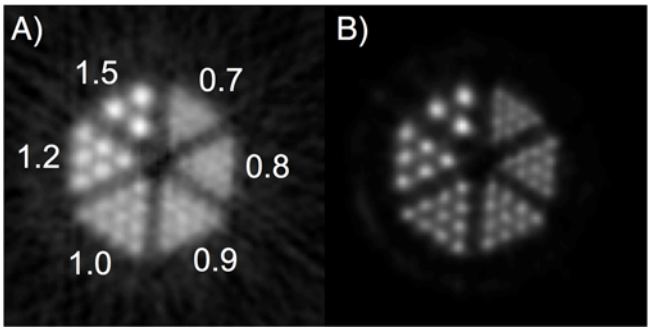

FIGURE 5. Reconstructions of a micro-resolution phantom made using (a) FBP-3DRP and (b) PSF-MLEM. Both images are cropped to a 32×32 mm^2 area. Insert diameter (in mm) is indicated in (a).

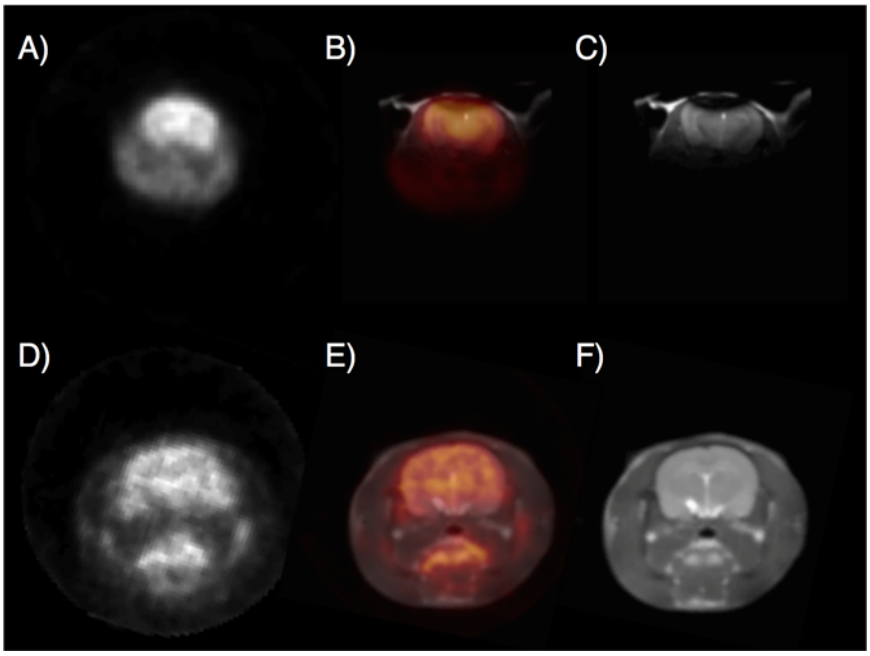

FIGURE 6. ^{18}F-FDG images of a mouse brain reconstructed with PSF-MLEM (a), shown fused with an MR image (b), with the un-fused MR image shown in (c). (d)-(f) show the corresponding sequence of images for the rat brain. All images are cropped to a 42×42 mm^2 area.

TABLES

TABLE 1
Summary of PET Insert Geometry and Features

Detector	
Photosensor	2×SensL ArraySB-4
Scintillator	Cerium-doped lutetium-yttrium oxyorthosilicate
Scintillator array dimensions	22×10 (bottom) + 21×9 (top)
Scintillator crystal size	1.2×1.2×6/4 mm^3 (bottom/top)
Crystal pitch	1.27 mm
Light-guide	1.0 mm of glass
System Geometry	
Detectors per ring	16
Detector ring diameter	65.8 mm
PET gantry inner diameter	60 mm
PET gantry outer diameter	113 mm
Axial FOV	27.94 mm
Transaxial FOV	~55 mm

TABLE 2
Spatial Resolution at the Axial Center of the FOV

Offset	FWHM (mm)			FWTM* (mm)			Vol.
(mm)	Radial	Tang.	Axial	Radial	Tang.	Axial	(μL)
0	1.17	1.35	1.36	2.43	3.23	2.70	2.15
5	1.27	1.45	1.30	2.62	3.27	2.67	2.38
10	1.53	1.49	1.38	3.36	3.31	2.82	3.13
15	1.86	1.46	1.49	4.16	3.40	3.04	4.06

*Full-width-at-tenth-maximum

TABLE 3
Spatial Resolution at ¼ Axial Offset from the Center of the FOV

Offset	FWHM (mm)			FWTM (mm)			Vol.
(mm)	Radial	Tang.	Axial	Radial	Tang.	Axial	(μL)
0	1.23	1.23	1.41	2.61	2.80	2.78	2.15
5	1.27	1.30	1.37	2.68	2.92	2.84	2.27
10	1.56	1.45	1.46	3.35	3.10	2.97	3.30
15	1.87	1.50	1.53	4.22	3.30	3.19	4.28

TABLE 4
Analysis of NEMA Image Quality Phantom

	Uniformity			Recovery-Coefficient			Spill-Over Ratio	
	FBP	PSF		FBP	PSF		FBP	PSF
Mean:	1.0	1.0	1 mm:	0.18±0.02	0.23±0.03	Air:	0.13±0.07	0.14±0.02
Max:	1.3	1.2	2 mm:	0.43±0.03	0.62±0.06	Water:	0.25±0.06	0.24±0.03
Min:	0.60	0.8	3 mm:	0.64±0.03	0.78±0.07			
Std.	0.076	0.06	4 mm:	0.77±0.02	0.80±0.05			
			5 mm:	0.84±0.03	0.83±0.07			

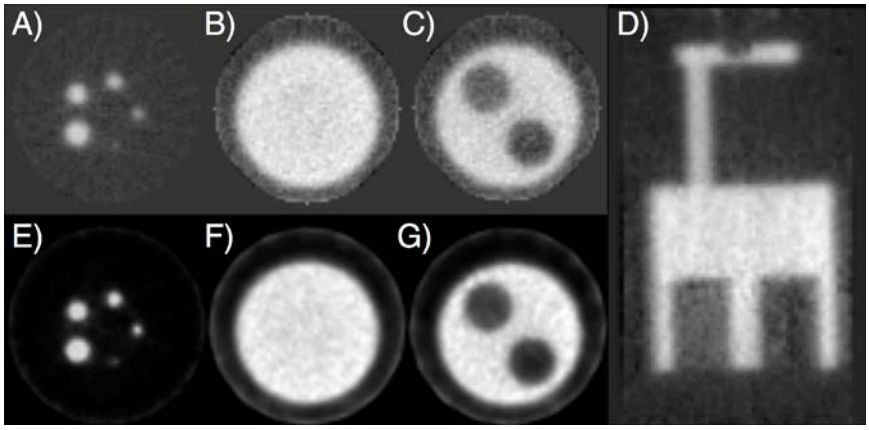

SUPPLEMENTAL FIGURE 1. Reconstructed images of the NEMA NU 4-2008 image quality phantom. Images (a)-(c) show the three sections of the phantom reconstructed with FBP-3DRP, and (e)-(g) reconstructed with PSF-MLEM, all 42×42 mm^2. Rod diameters are 1, 2, 3, 4, and 5 mm. Image (d) shows a 68×42 mm^2 axial section through the stitched-together FBP-3DRP reconstructions.

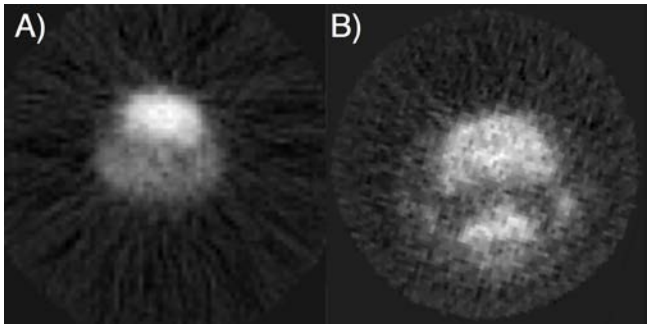

SUPPLEMENTAL FIGURE 2. ^{18}F-FDG images of a mouse brain (a) and a rat brain (b) reconstructed with FBP-3DRP, both 42×42 mm^2.